Supplement of Solid Earth, 15, 965–988, 2024
https://doi.org/10.5194/se-15-965-2024-supplement

Solid Earth Open Access EGU

Supplement of

Interseismic and long-term deformation of southeastern Sicily driven by the Ionian slab roll-back

Amélie Viger et al.

Correspondence to: Amélie Viger (amelie.viger.geo@gmail.com)

Supplementary Material

June 14, 2024

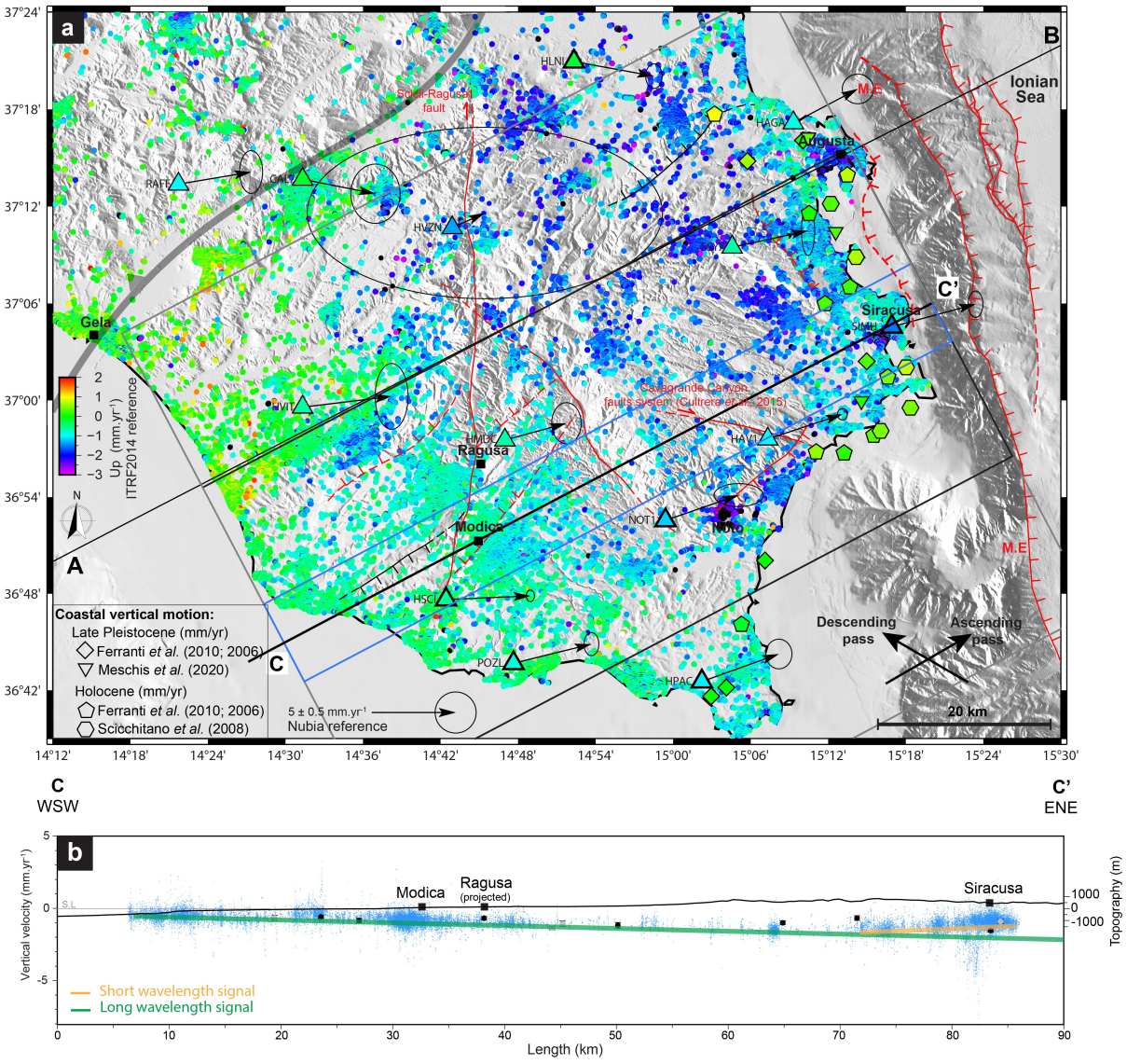

Figure S1: *Geodetics data available across the Hyblean Plateau region (see location in Figure 3). The Permanent-Scatterer (PS-InSAR) pseudo-3D Up velocities are from Henriquet et al., 2022, and were measured using Sentinel-1 satellite ascending and descending orbits acquired during the 2015-2020 period. GNSS 3D surface velocities are obtained from a reanalysis of the Nevada Geodetic Laboratory (NGL) data, including the time series of the year 2023 (Horizontal component reference: Fixed Nubia; Up component reference: ITRF2014). Coastal vertical motion during the Late Pleistocene and Holocene from Ferranti et al. (2006, 2010), Meschis et al. (2020), and Scicchitano et al. (2008). Major faults of the Hyblean Plateau and Malta Escarpment (M.E), including the offshore normal faults identified by Argnani and Bonazzi (2005), mapped by Gutscher et al. (2016) and analyzed by Gambino et al. (2021) (red: active fault; red dashed: inferred active fault; black: inactive fault). SW-NE trending velocity profile showing surface velocity (Up). PS-InSAR data were stacked across a 5 km width on both sides of the CC' profile (in blue). GNSS data were stacked using 20 km (in black) and 40 km (in gray) widths on both sides of the CC' profile. As for the AB profile (Figure 2b), vertical velocities show a long-wavelength signal (green line) and a short-wavelength signal in the East of the Hyblean Plateau (orange line). Topographic and bathymetric profiles are presented without vertical exaggeration (V.E.x1).*

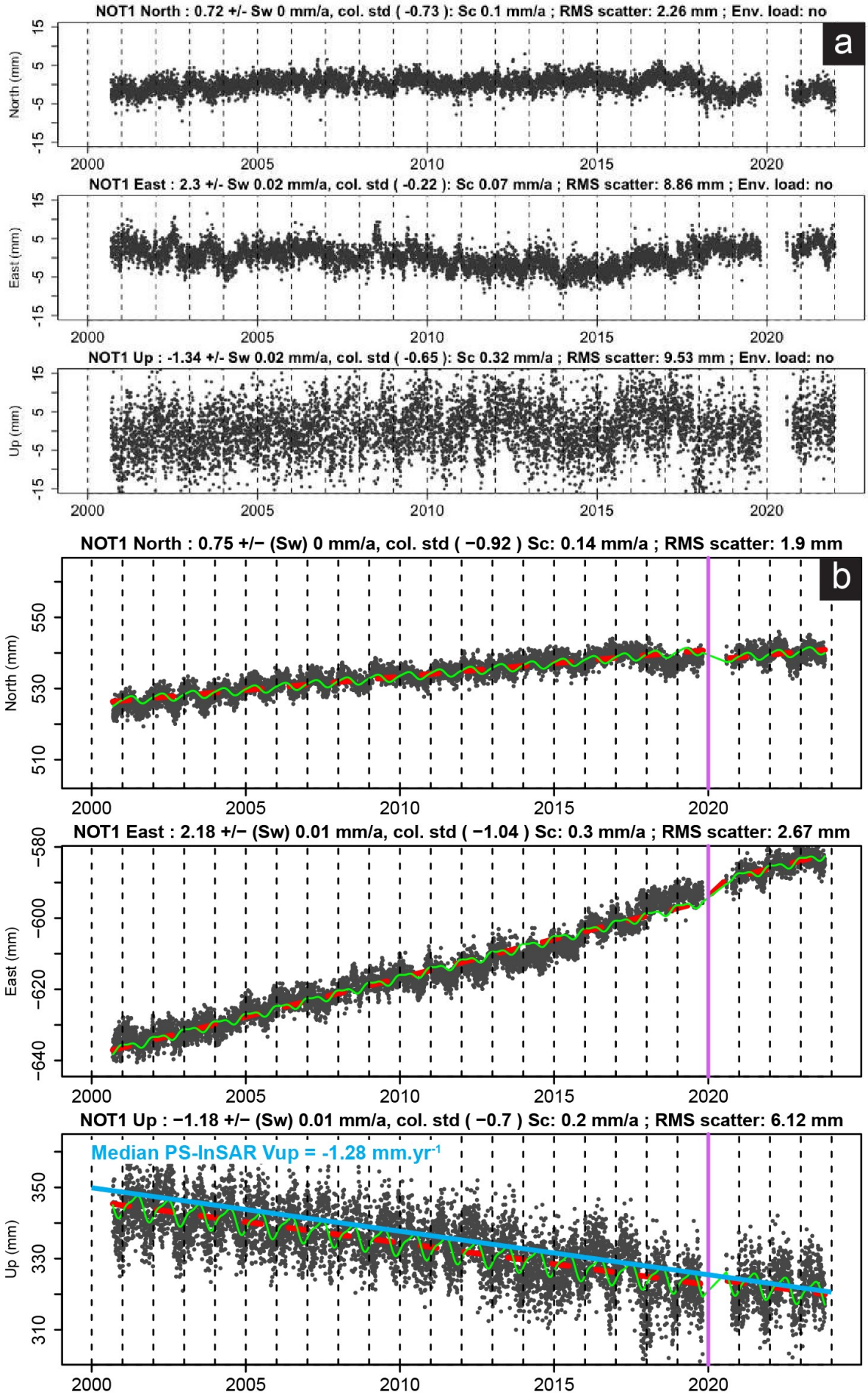
NOT1 North : 0.72 +/- Sw 0 mm/a, col. std (-0.73): Sc 0.1 mm/a ; RMS scatter: 2.26 mm ; Env. load: no
a
North (mm)
NOT1 East : 2.3 +/- Sw 0.02 mm/a, col. std (-0.22): Sc 0.07 mm/a ; RMS scatter: 8.86 mm ; Env. load: no
East (mm)
NOT1 Up : -1.34 +/- Sw 0.02 mm/a, col. std (-0.65): Sc 0.32 mm/a ; RMS scatter: 9.53 mm ; Env. load: no
Up (mm)
NOT1 North : 0.75 +/− (Sw) 0 mm/a, col. std (−0.92) Sc: 0.14 mm/a ; RMS scatter: 1.9 mm
b
North (mm)
NOT1 East : 2.18 +/− (Sw) 0.01 mm/a, col. std (−1.04) Sc: 0.3 mm/a ; RMS scatter: 2.67 mm
East (mm)
NOT1 Up : −1.18 +/− (Sw) 0.01 mm/a, col. std (−0.7) Sc: 0.2 mm/a ; RMS scatter: 6.12 mm
Median PS-InSAR Vup = -1.28 mm.yr-1
Up (mm)

Figure S2: *a) Raw times series of the NOT1 GNSS station for the North, East, and Up components. b) Time series models of the NOT1 GNSS station for the North, East, and Up components using inversion software from Masson et al. (2019). The linear trend appears in red. Periodic or seasonal and pluriannual effects appear in green. Corrected offsets are indicated by a purple vertical line. Data configuration above the signals: GNSS station name; component (North, East, or Up); velocity (mm/yr); white noise (Sw); noise color; colored noise (Sc); dispersion (RMS). GNSS time series were obtained from the Nevada Geodetic Laboratory (Blewitt et al., 2018). PS-InSAR vertical velocities (see Figure 2) are extracted over* $8\,\mathrm{km}^2$ *from the NOT1 station.*

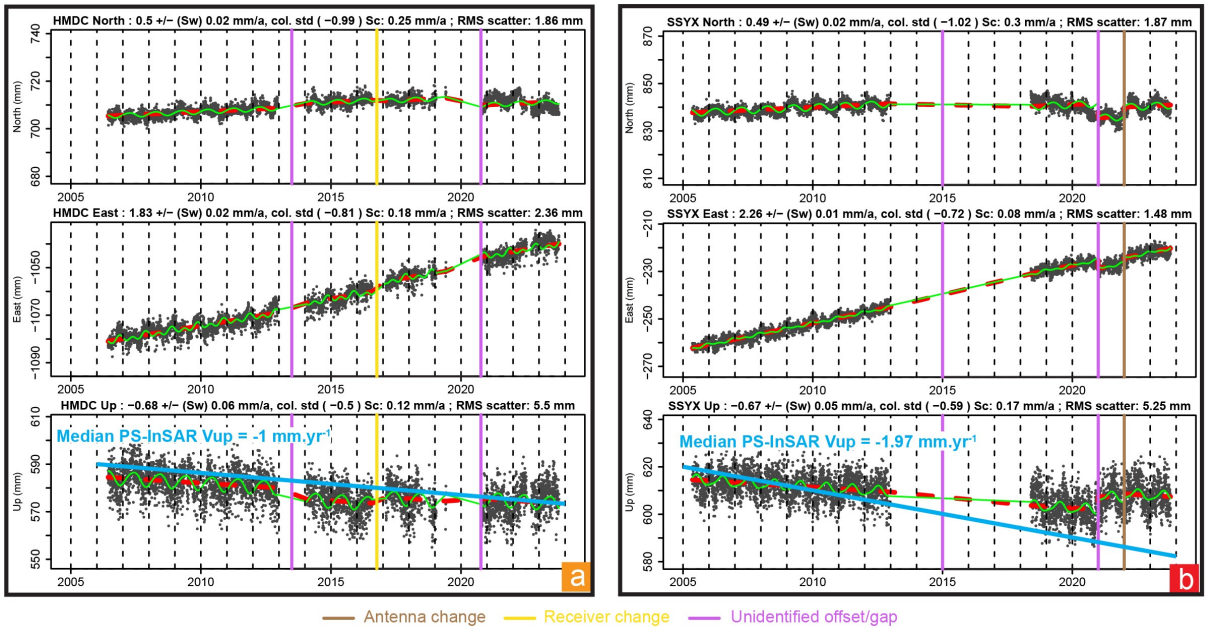

Figure S3: *Time series models of a) the HMDC GNSS station (shown in orange square due to the medium-quality of the time series); b) the SSYX GNSS station (shown in red square due to the low-quality of the time series) for the North, East, and Up components using software from Masson et al. (2019). The linear trend appears in red. Periodic or seasonal and pluriannual effects appear in green. Offset and/or gap are identified by receiver or antenna changes by Fabian et al., 2021. Data configuration above the signals; GNSS station name; component (North, East, or Up); velocity (mm/yr); white noise (Sw); noise color; colored noise (Sc); dispersion (RMS). Displacement data from the Nevada Geodetic Laboratory (Blewitt et al., 2018). PS-InSAR vertical velocities (see Figure 2) are extracted over* $8\,\mathrm{km}^2$ *from the SSYX and HMDC stations.*

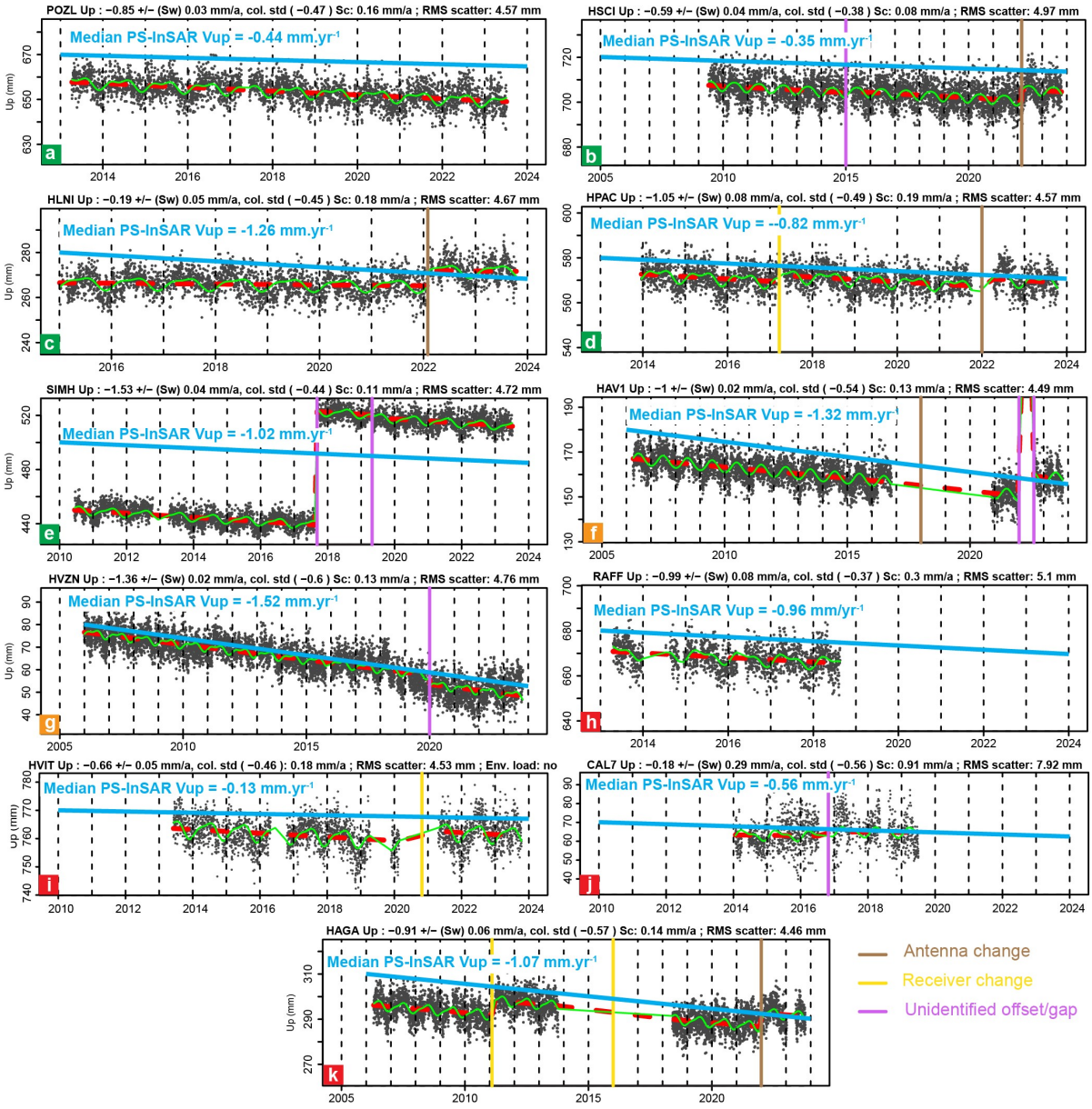

Figure S4: *a-e) Good-quality time series (> 8 years, few gaps and offsets) represented by a green square here and a thick GNSS station boundary in Figure 2a; f-g) Medium-quality time series (> 8 years with some gaps of several years and few offsets) shown in orange square; h-k) Low-quality time series (gaps of several years and high scattering) shown in red square; models of GNSS station Up component using inversion software from Masson et al. (2019). The linear trend appears in red. Periodic or seasonal and pluriannual effects appear in green. Corrected offsets are indicated indicated by a purple vertical line. Offset and/or gap are identified by receiver or antenna changes by Fabian et al., 2021. Data configuration above the signals: GNSS stations name; component (North, East, or Up); velocity (mm/yr); white noise (Sw); noise color; colored noise (Sc); dispersion (RMS). Displacement data from the Nevada Geodetic Laboratory (Blewitt et al., 2018). PS-InSAR vertical velocities (see Figure 2) are extracted over* $8\,\mathrm{km}^2$ *from the GNSS stations.*

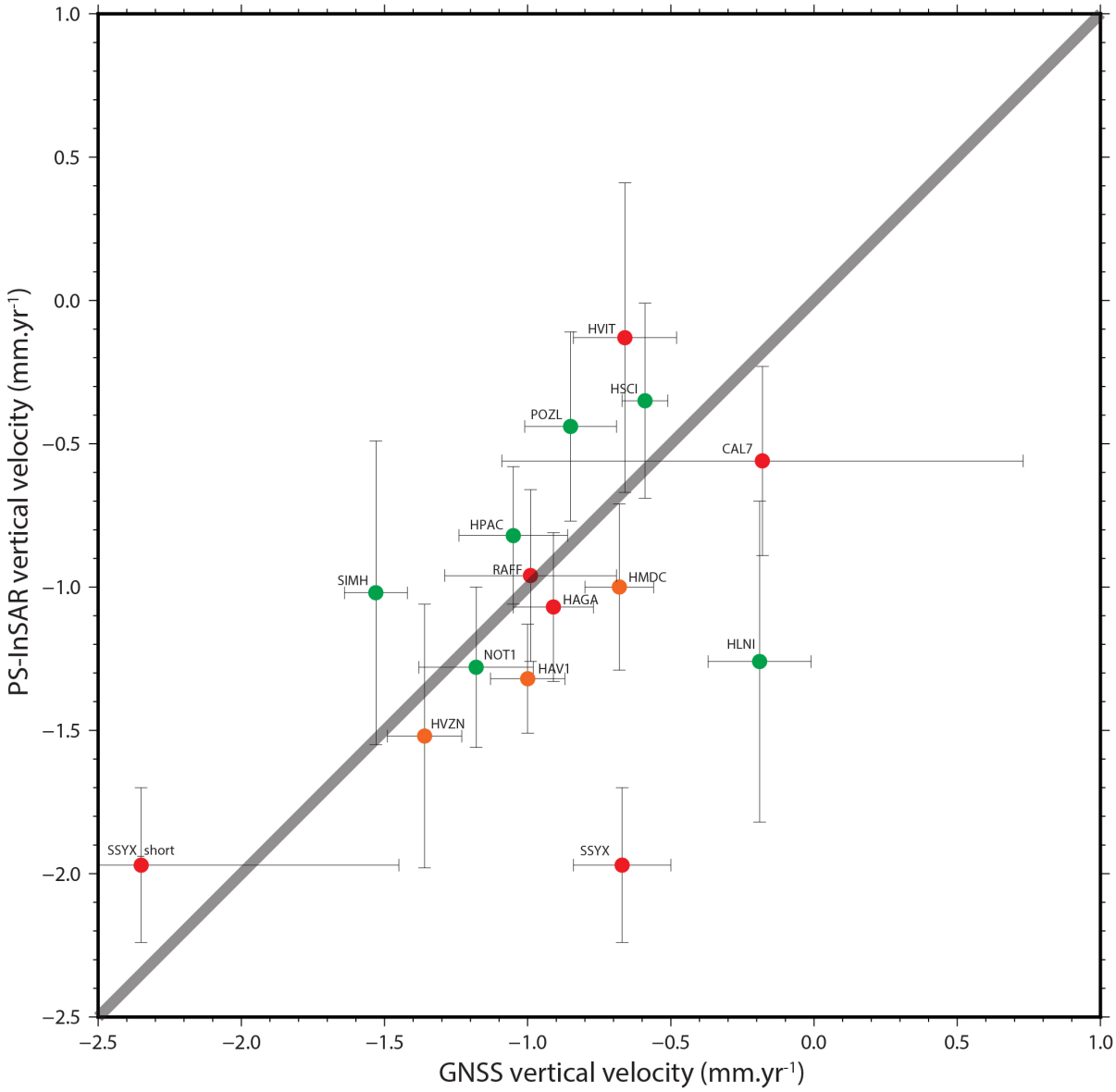

Figure S5: *Correlation between GNSS vertical velocity models and median of PS-InSAR vertical velocities (see Figure 2) extracted over* $8\,\mathrm{km}^2$ *from the GNSS stations. The uncertainty of PS-InSAR data is calculated with the average standard deviation of PS-InSAR data over* $8\,\mathrm{km}^2$ *around the GNSS station. In green is the good-quality time series (> 8 years, few gaps and offsets), in orange is the medium-quality time series (> 8 years, few gaps of several years and few offsets), and in red is the low-quality time series (gaps of several years and high scattering). The* $SSYX_{short}$ *means the SSYX time series of 2018-2023.*

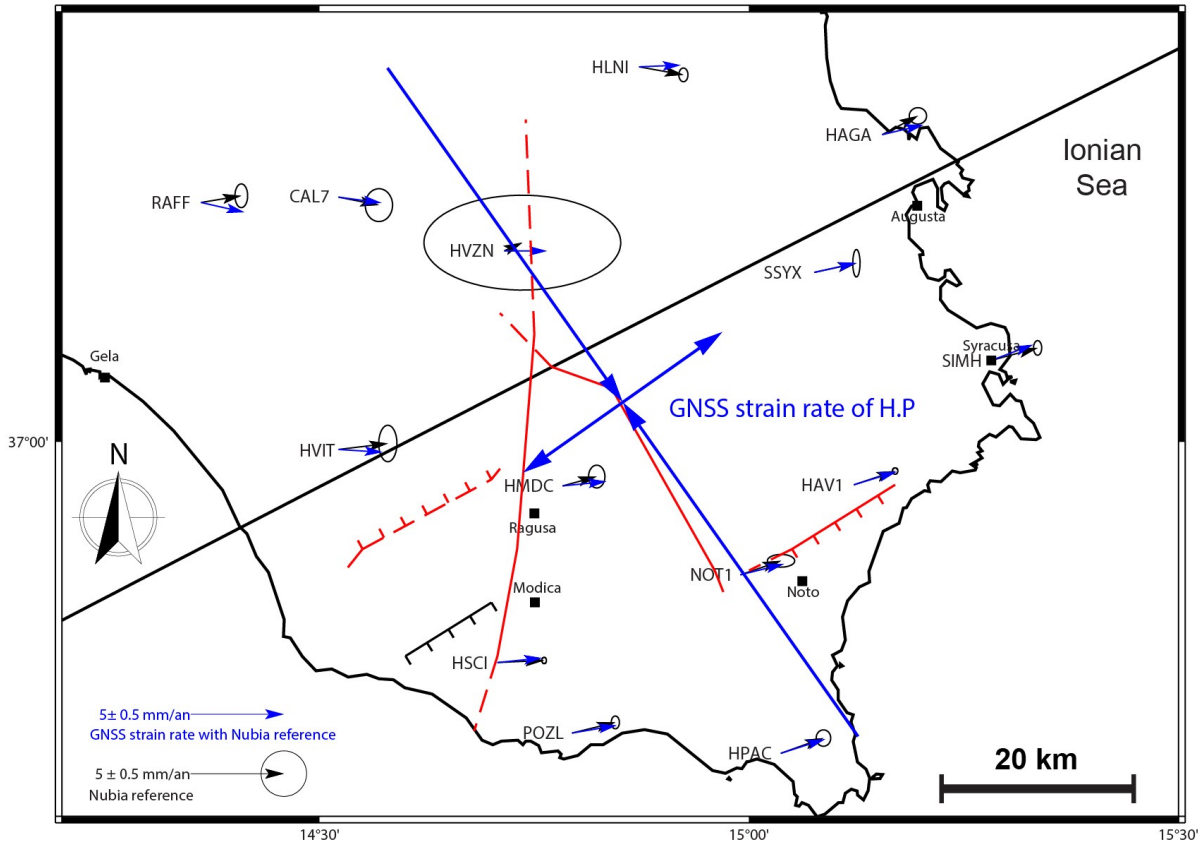

Figure S6: *Strain rate inversion of GNSS horizontal components (Figure 2) using the Mazzoti et al. (2005) software. Comparison between the GNSS strain rate inversion (blue vectors) and the GNSS horizontal component models (black vectors) for each GNSS station of Hyblean Plateau. The result of the global strain rate inversion over the Hyblean Plateau indicates an extension of 3.3e-9* yr^{-1} *oriented N55°E and a compression of* -1.1×10^{-8} yr^{-1} *oriented N145°E.*

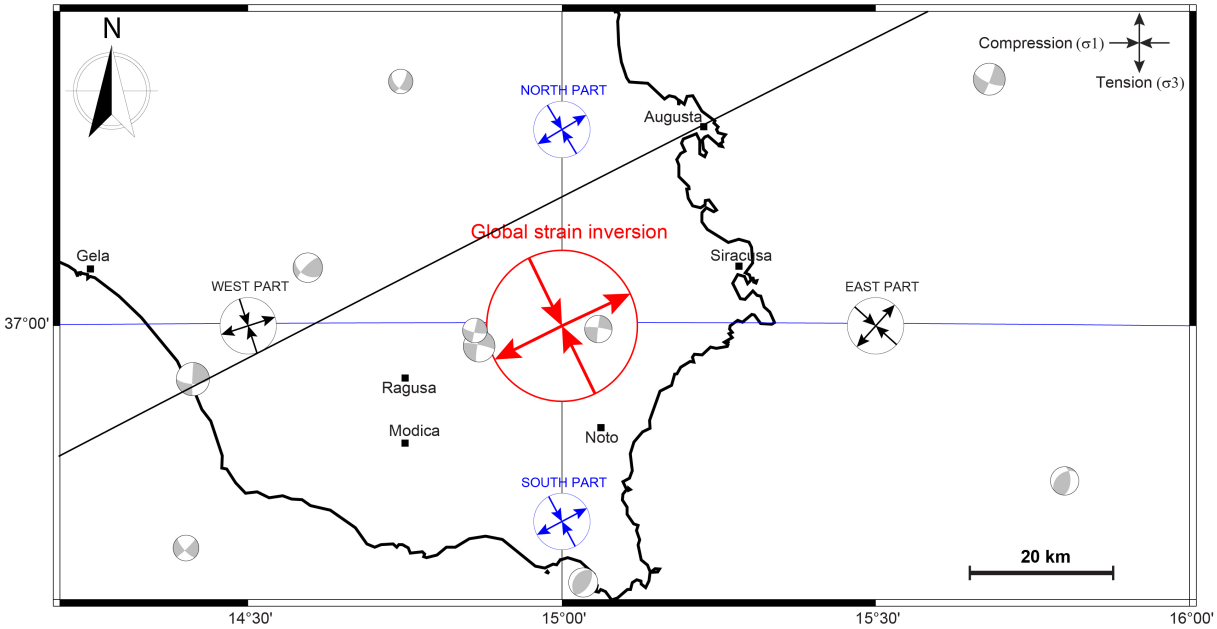

Figure S7: *Focal mechanisms inversion over Southeastern Sicily using Michael's method (Vavryčuk, 2014; Levandowski et al., 2018). The global strain inversion (red arrows) is consistent with the local strain inversion performed on four subregions dividing SE Sicily. North and South subregions are delimited by the blue line. West and East subregions are delimited by the black line.*

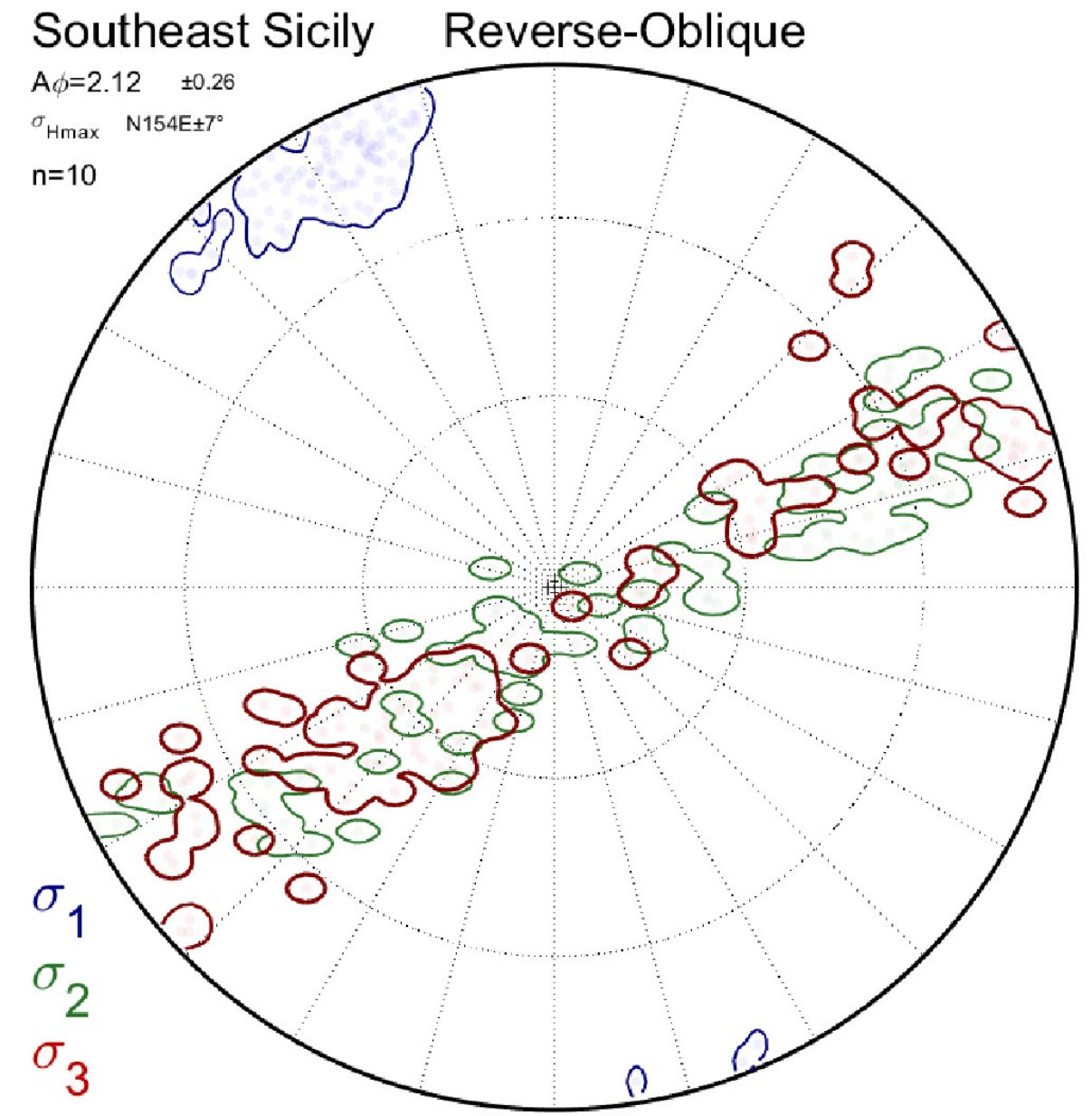

Figure S8: *Global stress tensor of focal mechanisms of Southeastern Sicily (Figure 3 and Supplementary Figure S7) using the Michael's method (Vavryčuk, 2014; Levandowski et al., 2018).*

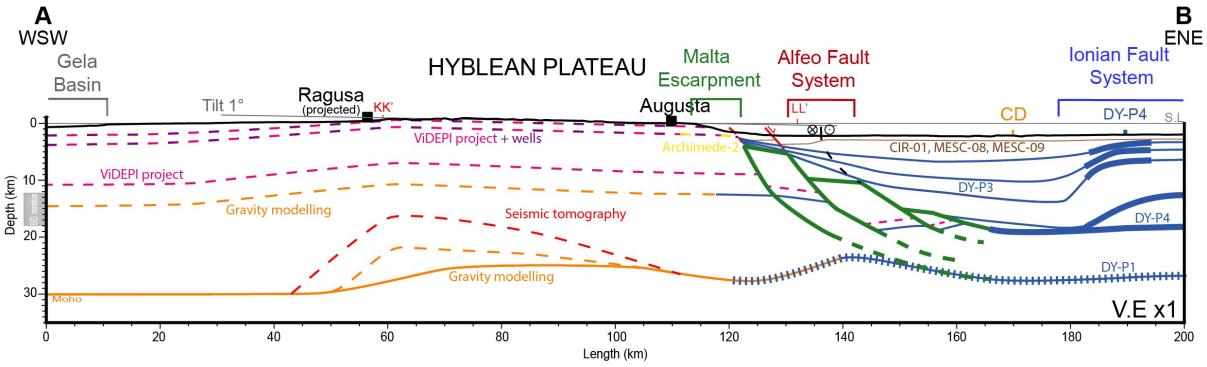

Figure S9: *Extents of the different data sets used to constrain the synthetic structural profile in Figure 4. Offshore, the seismic refraction isovelocities from Dellong et al., (2018, 2020) are represented in blue (thick dotted blue line for the DY-P1 profile, thick blue line for the DY-P4 profile, and blue line for the DY-P3 profile). The top of Messinian is represented in a brown line using seismic reflection CIR-01 profile from Gutscher et al. (2016), MESC-08, and MESC-09 profiles from Gambino et al. (2021, 2022). Onshore, the wells data from the ViDEPI project (in pink) and Lentini and Carbone (2014) (in purple) define the geometry of shallower geological layers, and wells data compilation from Lipparini et al. (2023) (in purple) constrains the top of the Triassic. The seismic reflection profile of Archimede 2 from Tugend et al. (2019), represented in yellow, indicates no outcrop of the Trias at the Malta Escarpment. The LL' and KK' seismic tomography profiles from Scarfì et al. (2018) (in red) show upwelling at ~15 km depth from the Moho of the Hyblean continental crust. The gravity modeling from Henriquet et al. (2019) (in orange) indicates an upwelling at ~20-25 km from the Moho of the Hyblean crust. Gravity modeling and the DY-P3 seismic refraction profile define the Brittle/Ductile transition of the Hyblean continental crust. The locations of all those datasets are indicated in Figure 4c. In green is our interpretation of tilted blocks using the DY-P3 seismic refraction profile (Dellong et al., 2018). Topography and depth are represented without vertical exaggeration (V.E.x1).*

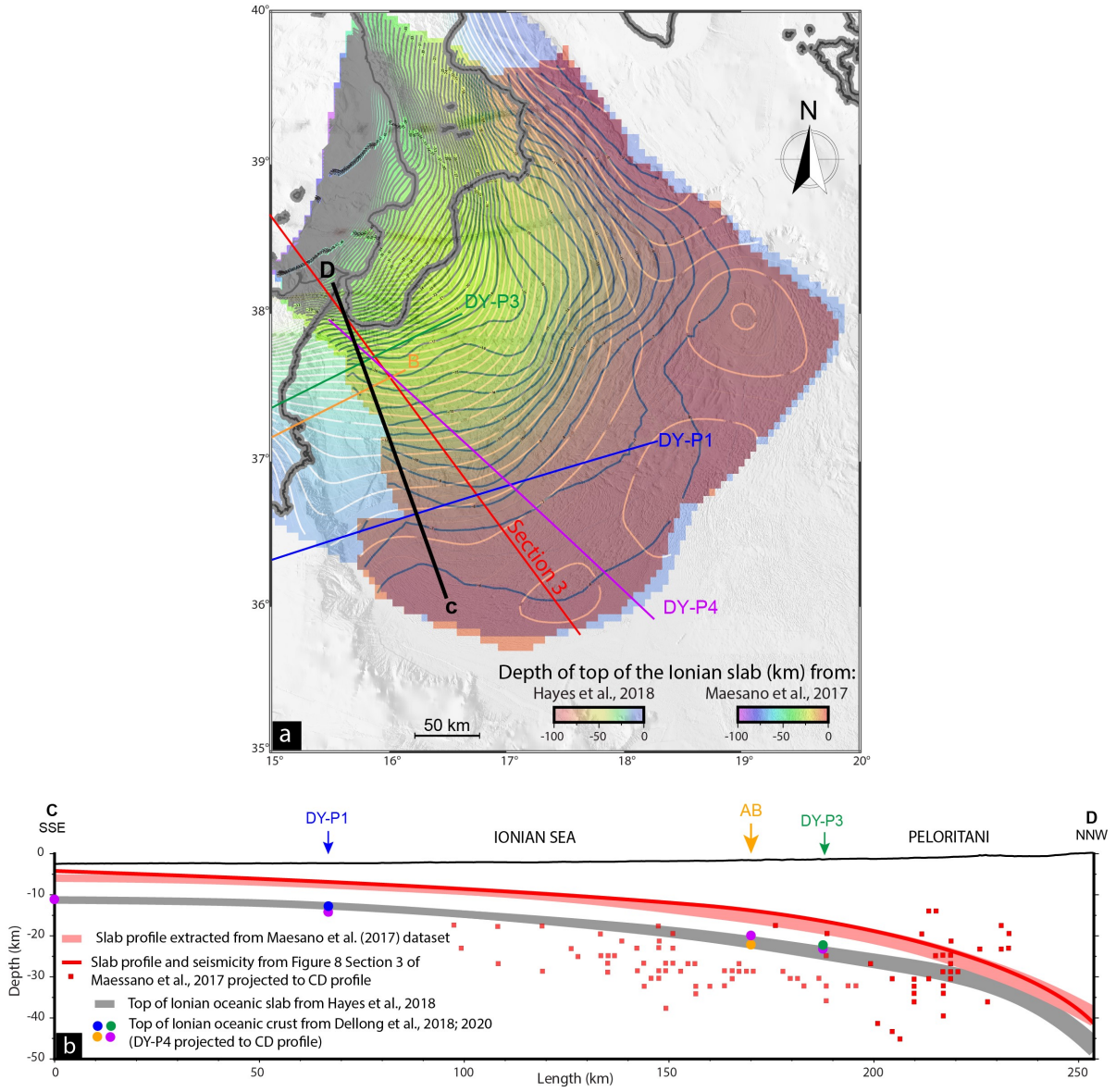

Figure S10: *a) Comparison of the Ionian slab geometries derived from Hayes et al. (2018) and Maessano et al. (2017) datasets with seismic refraction profile data from Dellong et al. (2018, 2020) in map view, and b) along the CD profile. The Ionian slab geometry of Maessano et al. (2017) takes into account the main décollement of the Calabrian subduction at the northern CD profile and a higher sedimentary cover in the southern CD profile, contrary to the Hayes et al. (2018) dataset takes into account the top of the Ionian crust all along the CD profile. The Hayes et al. (2018) dataset has a better correlation with the seismic refraction profiles from Dellong et al. (2018, 2020) (see Figure 5).*

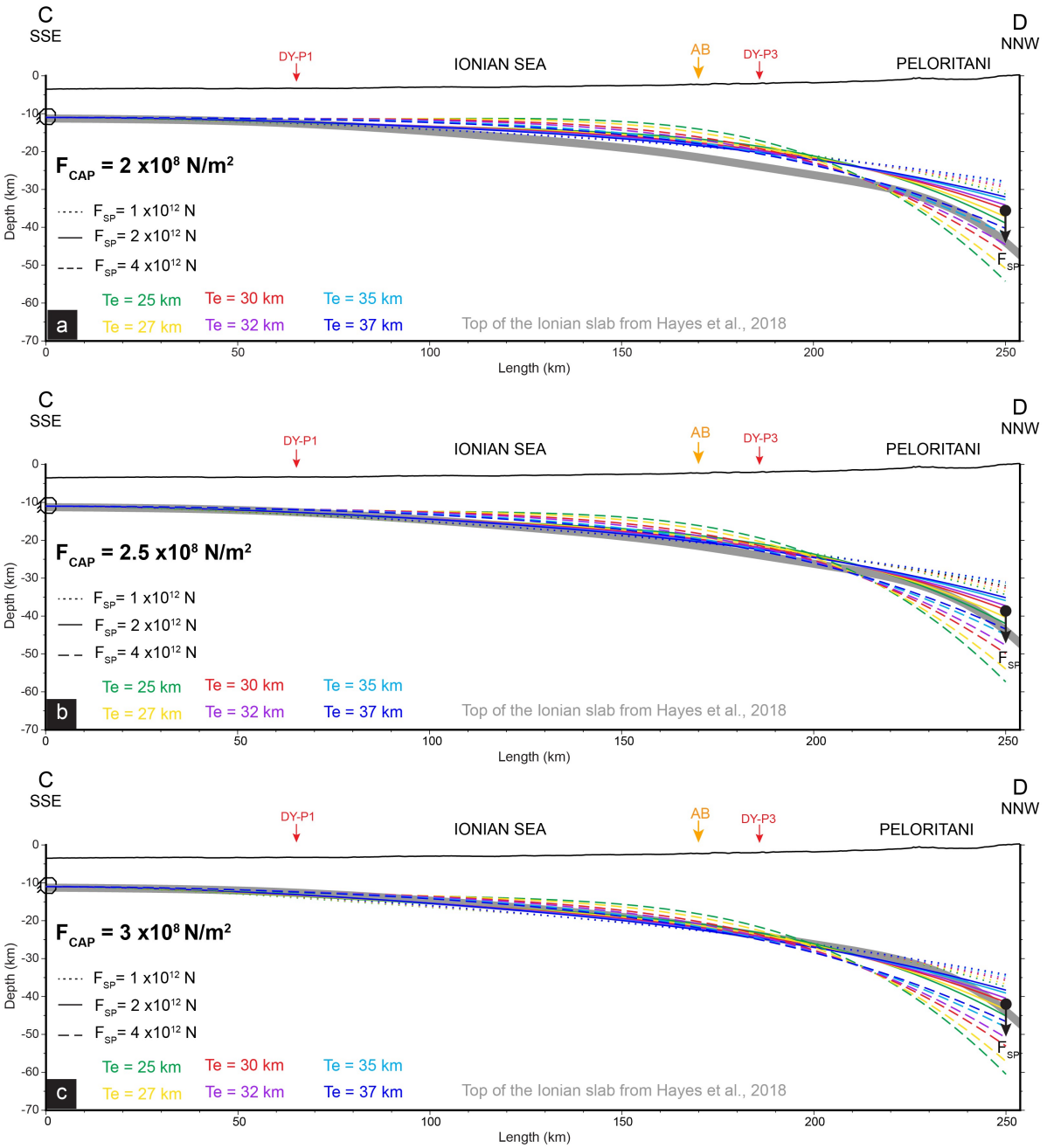

d F_{SP}	1 x10¹² N			2 x10¹² N			4 x10¹² N			
Te \ F_{CAP}	2 x10⁸ N/m²	2.5 x10⁸ N/m²	3 x10⁸ N/m²	2 x10⁸ N/m²	2.5 x10⁸ N/m²	3 x10⁸ N/m²	2 x10⁸ N/m²	2.5 x10⁸ N/m²	3 x10⁸ N/m²	
25 km	3.7	2.2	1.4	3	1.5	1.1	4.7	4.4	4.7	RMS (km)
27 km	3.8	2.3	1.5	3	1.3	0.9	4	3.7	4.1	
30 km	3.9	2.5	1.6	3	1.3	0.7	3.3	2.8	3.3	
32 km	4	2.5	1.7	3	1.4	0.8	2.9	2.3	2.8	
35 km	4.1	2.7	1.8	3.2	1.6	0.9	2.4	1.7	2.3	
37 km	4.2	2.8	1.8	3.3	1.7	1	2.3	1.3	2	

Figure S11: *The numerical models (gFlex from Wickert, 2016) of the oceanic lithosphere flexure were run with a broken plate with no-bending moment and no shear at the northern end of the CD profile, and a no-displacement condition at its southern end. The effects of the ante-Messinian cover and the CAP load are modeled as a linear gradient with a* $2500\,\mathrm{kg/m^2}$ *density and a maximum CAP load (F_{CAP}) a) of* $2 \times 10^8\,\mathrm{N/m^2}$*, b)* $2.5 \times 10^8\,\mathrm{N/m^2}$*, and c)* $3 \times 10^8\,\mathrm{N/m^2}$*. We performed a slab pull (F_B) of* $1 \times 10^{12}\,\mathrm{N}$ *(dotted lines),* $2 \times 10^{12}\,\mathrm{N}$ *(continuous lines), and* $4 \times 10^{12}\,\mathrm{N}$ *(dashed lines) bending of the oceanic lithosphere. We investigated elastic thickness (Te) ranging from 25 to 37 km for the same model parameters. We represented the model with an elastic thickness of 25 km (in green), 27 km (in yellow), 30 km (in red), 32 km (in purple), 35 km (in cyan), and 37 km (in blue). d) Misfit (RMS in km) of Ionian slab top depth (Hayes, 2018) (in gray) interpolated on each model. The shaded cells are models represented in Figure 5.*

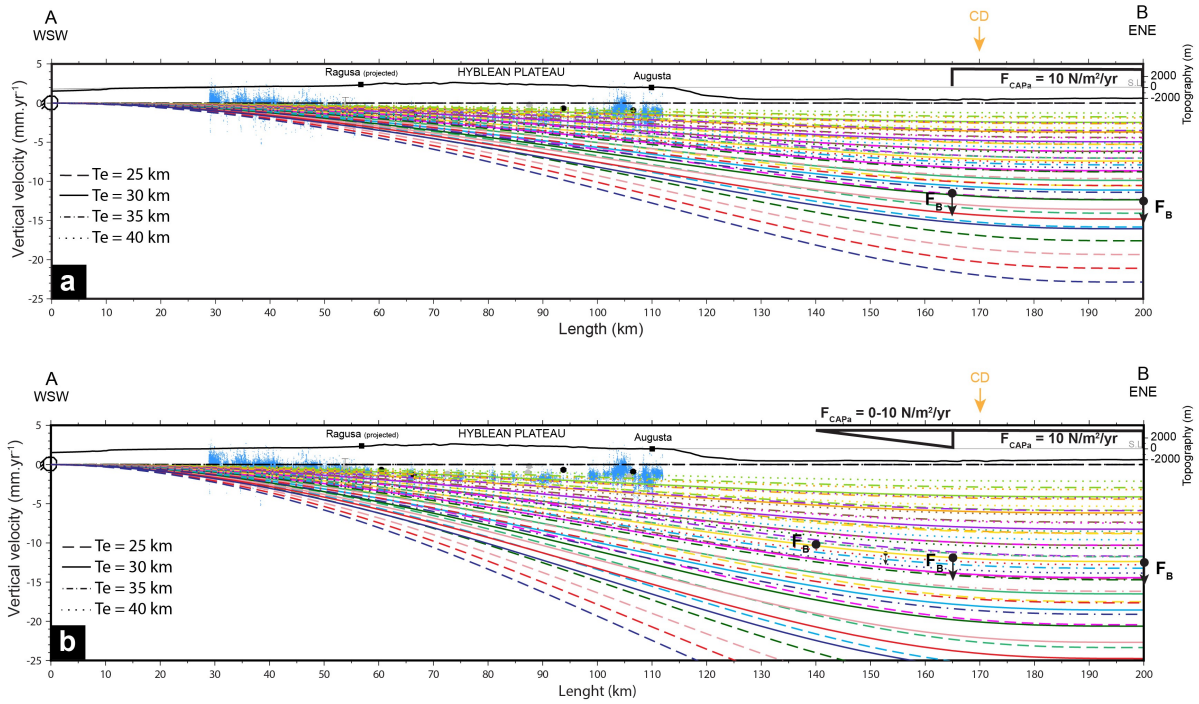

c			F_B (N/m/yr)											
	Te (km)	RMS (mm/yr)	1 x10⁴	1.5 x10⁴	2 x10⁴	2.5 x10⁴	3 x10⁴	3.5 x10⁴	4 x10⁴	4.5 x10⁴	5 x10⁴	5.5 x10⁴	6 x10⁴	6.5 x10⁴
Constant on 165-200	25	InSAR	0.5	0.7	1.2	1.7	2.3	2.8	3.4	4	4.5	5.1	5.6	6.2
		GNSS	*1.2*	*1.7*	*2.2*	*2.8*	*3.4*	*3.9*	*4.5*	*5*	*5.6*	*6.2*	*6.7*	*7.3*
	30	InSAR	0.6	0.5	0.7	1	1.4	1.8	2.3	2.7	3.1	3.5	3.9	4.4
		GNSS	*0.9*	*1.3*	*1.7*	*2.1*	*2.5*	*2.9*	*3.4*	*3.8*	*4.2*	*4.6*	*5.1*	*5.5*
	35	InSAR	0.7	0.5	0.5	0.6	0.8	1.1	1.4	1.7	2	2.3	2.6	2.9
		GNSS	*0.7*	*1*	*1.3*	*1.6*	*1.9*	*2.2*	*2.5*	*2.8*	*3.1*	*3.4*	*3.7*	*4*
	40	InSAR	0.9	0.7	0.5	0.5	0.5	0.6	0.8	1	1.2	1.4	1.6	1.9
		GNSS	*0.6*	*0.8*	*1*	*1.2*	*1.4*	*1.6*	*1.8*	*2.1*	**2.3**	*2.5*	*2.7*	*3*
Gradually on 140-165 + Constant on 165-200	25	InSAR	0.9	1.9	2.9	3.8	4.8	5.8	**6.9**	7.9	8.9	9.9	10.9	11.9
		GNSS	*2*	*3*	*4*	*5*	*6*	*7*	*8*	*9*	*10*	*11*	*12*	*13*
	30	InSAR	0.5	1.1	1.9	2.6	3.3	4.1	4.8	5.6	6.3	7.1	7.8	8.6
		GNSS	*1.5*	*2.2*	*3*	*3.7*	*4.5*	*5.2*	*6*	*6.7*	*7.5*	*8.2*	*9*	*9.7*
	35	InSAR	0.5	0.6	1.1	1.6	2.2	2.7	3.2	3.8	4.3	4.9	5.4	6
		GNSS	*1.1*	*1.6*	*2.2*	*2.7*	*3.3*	*3.8*	*4.4*	*4.9*	*5.5*	*6*	*6.6*	*7.1*
	40	InSAR	0.6	0.5	0.6	0.9	1.3	1.7	2.1	2.5	2.9	3.3	3.7	4.1
		GNSS	*0.9*	*1.2*	*1.6*	*2*	*2.4*	*2.8*	*3.2*	**3.6**	*4*	*4.4*	*4.8*	*5.2*

Figure S12: *Continental crustal flexure is controlled by the southward retreat of the Ionian slab. We calculated the flexure (gFlex from Wickert, 2016) induced by the only CAP load (F_{CAPa}) of* $10\,\mathrm{N/m^2/yr}$ *distributed on the COT (in black), and on the adjacent Ionian crust (in white). For an elastic thickness ranging from 25 to 40 km, models have bending forces (F_B) of* $1\times10^4\,\mathrm{N/m/yr}$ *(in light green),* $1.5\times10^4\,\mathrm{N/m/yr}$ *(in orange),* $2\times10^4\,\mathrm{N/m/yr}$ *(in purple),* $2.5\times10^4\,\mathrm{N/m/yr}$ *(in brown),* $3\times10^4\,\mathrm{N/m/yr}$ *(in yellow),* $3.5\times10^4\,\mathrm{N/m/yr}$ *(in magenta),* $4\times10^4\,\mathrm{N/m/yr}$ *(in turquoise),* $4.5\times10^4\,\mathrm{N/m/yr}$ *(in light blue),* $5\times10^4\,\mathrm{N/m/yr}$ *(in dark green),* $5.5\times10^4\,\mathrm{N/m/yr}$ *(in pink),* $6\times10^4\,\mathrm{N/m/yr}$ *(in red), and* $6.5\times10^4\,\mathrm{N/m/yr}$ *(in dark blue) distributed on a) the only adjacent Ionian crust (165 to 200 km marks of the AB profile) as a constant load, and b) including also part of the COT (140 to 165 km marks of the AB profile) as a linear load gradient evolving from zero to the maximum calculated CAP load and bending force (see above). PS-InSAR vertical velocities (in blue) and GNSS vertical velocities with their uncertainties. Topographic and bathymetric profiles are presented without vertical exaggeration (V.E.x1). c) Misfit (RMS in mm/yr) of the PS-InSAR and GNSS (see b) interpolated on different models. The shaded cells are the best models according to the RMS PS-InSAR value, and these models are represented in Figure 6b.*

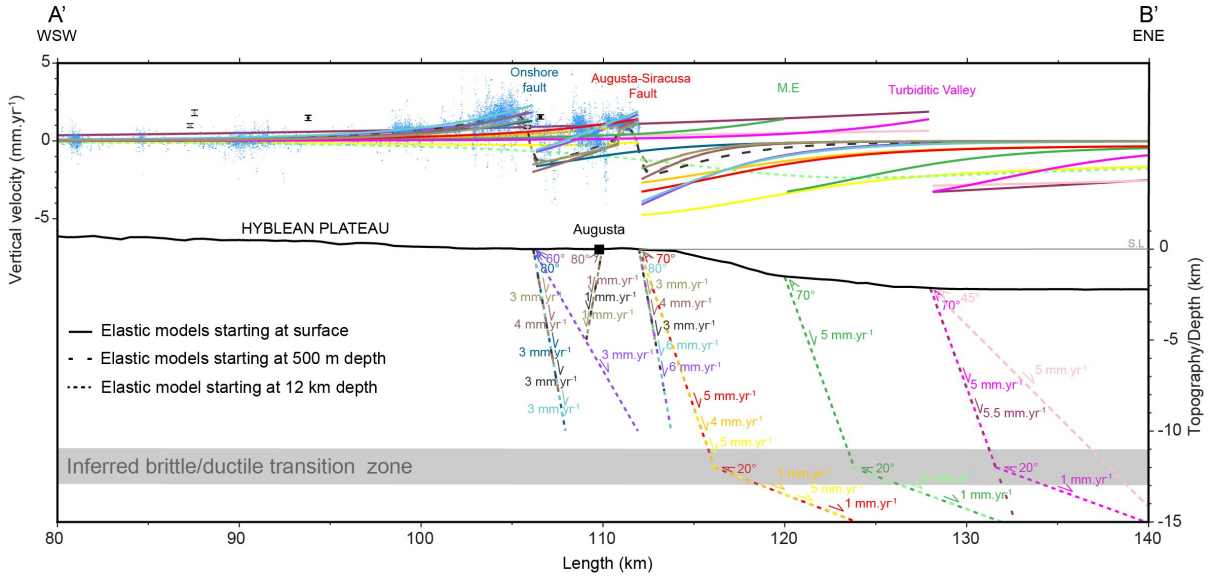

Figure S13: *Numerical interseismic load models (Coulomb 3.4) of inferred active or active normals faults offshore the east of the Hyblean Platform have a step size of 100 meters. Profile of PS-InSAR velocities Up (in blue) are the reference frame for models and were stacked across a 5 km width on both sides of the AB profiles in Figure 7b (in blue). Modeled elastic deformation: the Turbiditic Valley normal fault (magenta, dark pink, and pink lines); the Malta Escarpment (M.E) (green and light green lines); the Augusta-Siracusa coastal fault (red, orange, and yellow lines); onshore inferred active faults in Augusta (dark blue line). Modeled interseismic deformation; the Augusta-Siracusa coastal fault plus onshore inferred active faults are represented in light blue, dark, and light brown lines. Topography and depth are drawn without vertical exaggeration (V.E.x1).*

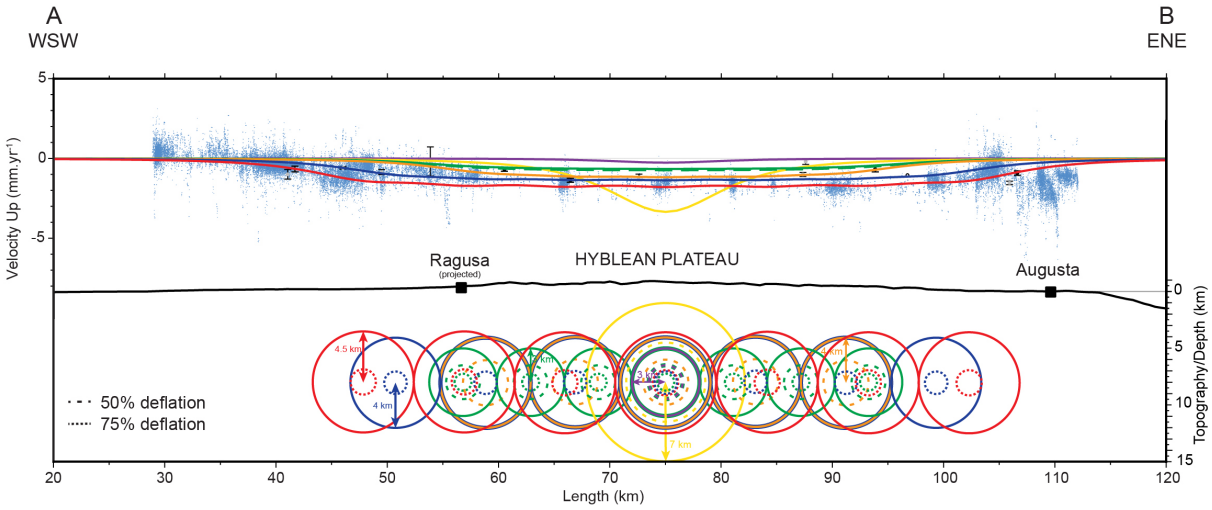

Figure S14: *Model of volcanic material deflation (Mogi, 1958) in central Hyblean Plateau. Volcanic material is represented by a sphere or several spheres located at 8 km depth according to Henriquet et al. (2019). We perform a sphere of 3 km radius (in purple) and 7 km (in yellow) with a deflation of 50% (dashed purple and yellow lines). We also test seven spheres of a 3 km radius (in green) with a deflation of 50% (dashed green line) and 75% (dotted green line). We perform five sphere of 4 km radius (in orange) with a deflation of 50% (dashed orange line). We test seven spheres of 4 km radius (in blue) with a deflation of 75% (dotted blue line). We also perform seven spheres of 4.5 km radius (in red) with a deflation of 75% (dotted red line). Recent PS-InSAR velocities Up (in blue) and GNSS velocities Up (NGL) with their uncertainties stacked at 20 km (in black) and 40 km (in gray) along the AB profile (see location in Figure 2). Topography and depth are represented without vertical exaggeration (V.E.x1).*

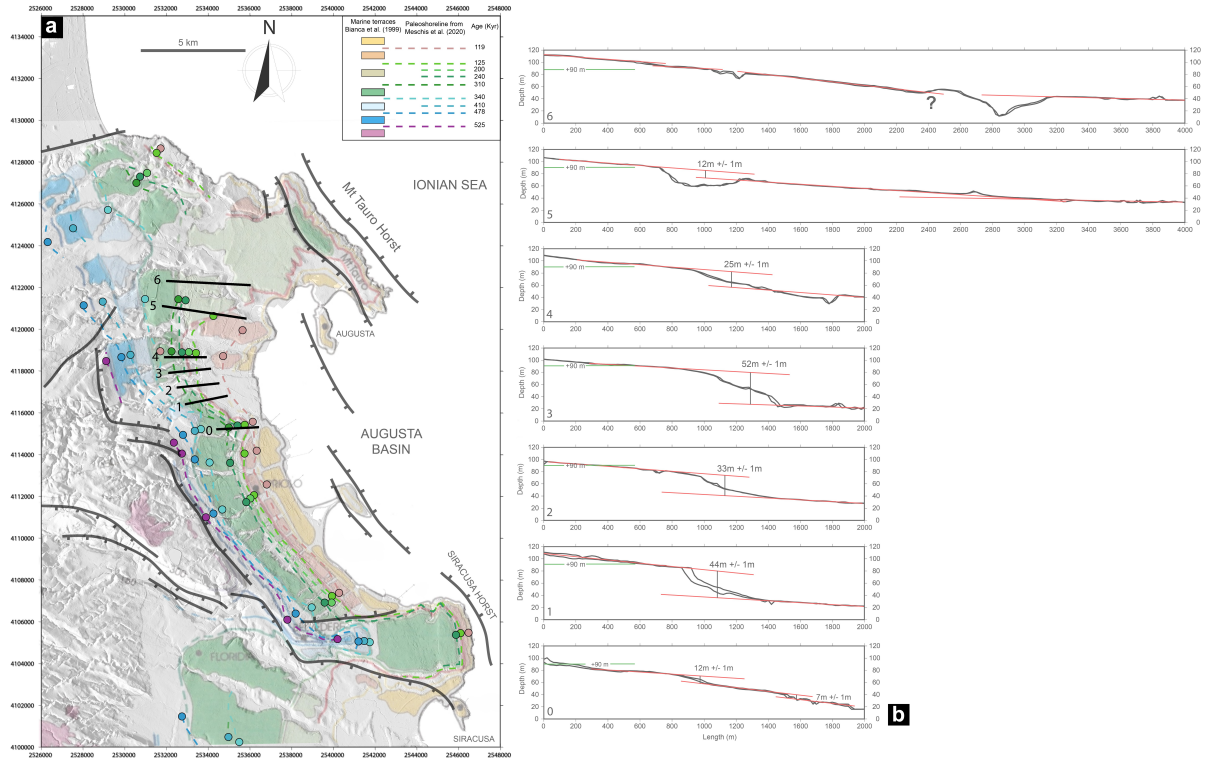

Figure S15: *Simplified structural map of the Augusta-Siracusa coastal region showing: a) in cartographic view, the series of uplifted marine terraces mapped by Bianca et al. (1999) and dated by Dutton et al. (2009) and Meschis et al. (2020); b) topographic profiles, with indication of offset amplitudes, across the potential tectonic fault/fold scarps (in red, Figure 9c).*